

# Subwavelength integrated photonics

Pavel Cheben<sup>1\*</sup>, Robert Halir<sup>2,3</sup>, Jens H. Schmid<sup>1</sup>, Harry A. Atwater<sup>4</sup> & David R. Smith<sup>5</sup>

**In the late nineteenth century, Heinrich Hertz demonstrated that the electromagnetic properties of materials are intimately related to their structure at the subwavelength scale by using wire grids with centimetre spacing to manipulate metre-long radio waves. More recently, the availability of nanometre-scale fabrication techniques has inspired scientists to investigate subwavelength-structured metamaterials with engineered optical properties at much shorter wavelengths, in the infrared and visible regions of the spectrum. Here we review how optical metamaterials are expected to enhance the performance of the next generation of integrated photonic devices, and explore some of the challenges encountered in the transition from concept demonstration to viable technology.**

A periodic crystal lattice acts like a diffraction grating for X-rays with wavelengths comparable to the lattice constant, but appears like a homogeneous medium for light of the much longer optical wavelengths. Similarly, a dielectric grating can diffract light or behave as an equivalent homogeneous medium, depending on the ratio of the wavelength of the light to the periodicity of the grating. In a subwavelength grating (SWG), the fundamental dielectric building blocks, which are arranged periodically, assume the role of the atoms of the crystal lattice and ultimately determine the macroscopic optical properties of the metamaterial. Indeed, if the period of the grating is much smaller than the wavelength of the light, diffraction effects are suppressed, and the structure behaves like a homogeneous anisotropic material with an equivalent anisotropic permittivity tensor<sup>1</sup> with respect to the macroscopic electromagnetic field. Artificial media with optical properties synthesized by deliberate structuring have been used for over 50 years in diffractive free-space optics<sup>2,3</sup>. Some early subwavelength structures were also used in semiconductor multilayers<sup>4</sup> and waveguides<sup>5</sup> for phase-matched nonlinear frequency conversion. The term ‘metamaterial’ was coined more recently<sup>6–8</sup>, and originally referred to artificial media designed to have a greater range of material properties than those available in nature. Metamaterials based on metallic structures were subsequently developed to demonstrate exotic properties—such as negative permeability and permittivity<sup>9</sup>, super-resolution<sup>7</sup>, invisibility<sup>10</sup> and asymmetric transmission<sup>11</sup>—or in the quest for optical magnetism<sup>12</sup>. Current metamaterial research includes the study of metallic, hybrid metallic–dielectric and all-dielectric nanostructures, leading to new photonic device concepts, which have been described in several comprehensive review articles<sup>13–22</sup>.

In this review we discuss how bringing metamaterials into optical-waveguide technologies and on-chip architectures provides new degrees of freedom to control the flow of light in integrated photonic devices. We emphasize the role of SWGs in silicon-based integrated optical circuits<sup>23</sup>, which are considered to be key components for the development of the next generation of optical communication, biomedical, quantum and sensing technologies.

Subwavelength-grating metamaterial structures were recently implemented in silicon waveguides<sup>24–26</sup>, allowing accurate lithographic control over the distribution of the electromagnetic field and the wavevector of the propagating modes<sup>27</sup>. Through the realization of practical components at telecommunication wavelengths, it was demonstrated that waveguide mode transformation can be controlled by changing the effective material index, achieving a broad wavelength range with a negligible level of scattering loss<sup>28,29</sup>. Independently, Levy et al.<sup>30</sup> showed that a spatially

inhomogeneous metamaterial can be used to control the effective index of refraction in a silicon slab waveguide. A unique aspect of the slab waveguide configuration is the large degree of control in creating a wide range of different spatial distributions of metamaterial refractive index by lithographic nano-patterning. This level of control has been demonstrated on various integrated devices, including the waveguide lens<sup>30</sup>, the invisibility cloak<sup>31</sup>, a flattened Luneburg lens<sup>32</sup>, Maxwell’s fish-eye lens<sup>33</sup> and dual-function ‘Janus’ devices<sup>34</sup>.

The emerging opportunity to control the properties of integrated optical structures at the subwavelength scale has motivated intense research efforts, and a plethora of advanced devices with unprecedented performance have been demonstrated<sup>27,28,30,35–42</sup>. Such subwavelength devices can be fabricated in the same lithography step as conventional waveguides by using manufacturing processes that are well established in the semiconductor electronics industry, thus making their integration straightforward. Highly efficient subwavelength structures for coupling light into integrated photonic devices have been developed, including subwavelength-engineered edge couplers<sup>36,43</sup> and surface grating couplers hybridized with optical metasurfaces<sup>40,44,45</sup> at both near-infrared (telecommunication) and mid-infrared wavelengths. Subwavelength systems for sensing<sup>39,46,47</sup>, and even an electronic–photonic system integrating transistors and nanostructured optical elements<sup>48</sup> on a single chip, have been demonstrated.

In the following, we review diverse implementations of subwavelength-engineered structures in integrated optics. We begin by summarizing the physical principles of SWG metamaterial structures related to the operation of integrated photonic platforms. Next, we describe the state of the art of metamaterial devices in silicon-on-insulator waveguides and analyse the arising challenges vis-à-vis the development of viable photonic integrated technology. We emphasize the need for functional metamaterial photonic elements that can be integrated on a single platform, interface easily with the external input and output and are compatible with established semiconductor nanofabrication processes and integrated-optics material systems. Finally, we outline exciting new applications and research directions.

## Principles of SWGs

In the simplest case, an SWG consists of periodically arranged dielectric particles with dimensions much smaller than the wavelength, which form an array of Rayleigh scatterers. For conceptual insight into the optical properties of non-resonant metamaterial structures, a good starting point is the treatment of light propagation through

<sup>1</sup>National Research Council Canada, Ottawa, Ontario, Canada. <sup>2</sup>Universidad de Málaga, Departamento de Ingeniería de Comunicaciones, ETSI Telecomunicación, Málaga, Spain. <sup>3</sup>Bionand Center for Nanomedicine and Biotechnology, Málaga, Spain. <sup>4</sup>California Institute of Technology, Pasadena, CA, USA. <sup>5</sup>Duke University, Durham, NC, USA. \*e-mail: pavel.cheben@nrc.ca

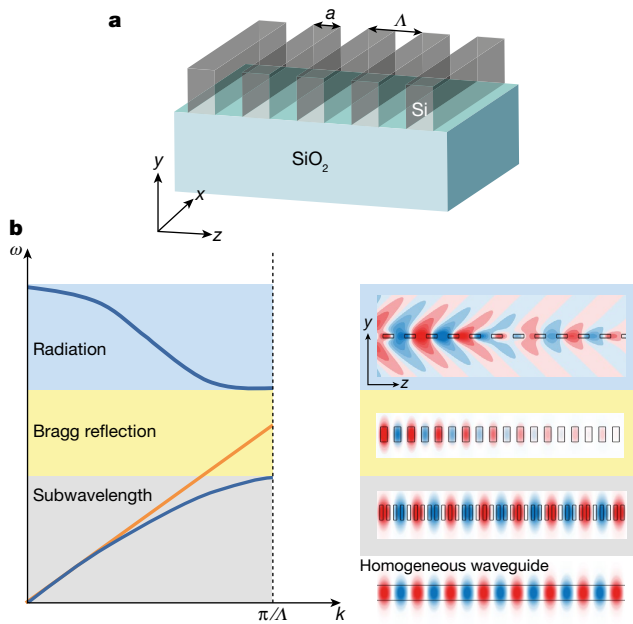


**Fig. 1 | Light propagation through a periodic dielectric structure.** **a**, Silicon-on-insulator slab waveguide with etched longitudinal or transverse SWG (for light propagation along the  $z$  or  $x$  axis, respectively). **b**, Schematic dispersion diagram (left) and corresponding electric field profiles (right) of a periodic slab waveguide for the three regimes of subwavelength-guided wave propagation, Bragg reflection and radiation. In the dispersion diagram, the red line is the dispersion of a homogeneous waveguide with an equivalent core refractive index. In the right panel, positive values of the electric field are shown in blue, negative values in red and zero values in white. The black rectangles represent silicon segments.

a finely stratified medium proposed by Rytov<sup>1</sup>, where a simple one-dimensional periodic structure consisting of alternating slabs of dielectric materials with refractive indices  $n_1$  and  $n_2$  is considered. It is well known that such a periodic structure can act as a diffraction grating. Rytov found that if the grating period is much smaller than the wavelength of the light, the SWG is optically equivalent to a uniaxial crystal with optic axis perpendicular to the layers. Light incident on the grating can have electric field polarization parallel or perpendicular to the periodic interfaces, and the respective equivalent refractive indices are given by:

$$\begin{aligned} n_{\parallel}^2 &\approx \frac{a}{\Lambda} n_1^2 + \left(1 - \frac{a}{\Lambda}\right) n_2^2 + \mathcal{O}\left(\frac{\Lambda^2}{\lambda^2}\right) \\ n_{\perp}^2 &\approx \frac{a}{\Lambda} n_1^{-2} + \left(1 - \frac{a}{\Lambda}\right) n_2^{-2} + \mathcal{O}\left(\frac{\Lambda^2}{\lambda^2}\right) \end{aligned} \quad (1)$$

Here,  $a$  is the width of a slab of material with index  $n_1$ ,  $\Lambda$  is the grating period and  $\lambda$  is the free-space wavelength. In the long-wavelength limit, the refractive index approaches a static value with correction terms of the order of  $\Lambda^2/\lambda^2$ . This treatment of the grating structure as an equivalent homogeneous material is also referred to as homogenization or effective-medium theory<sup>2,3,16</sup>. We note that the refractive index of the equivalent homogeneous material is polarization-dependent, that is, the material is birefringent.

Over the past decades, fabrication technology has progressed to a point where thin dielectric or metallic films deposited on substrates can be routinely patterned with structures of dimensions that are substantially smaller than the wavelength of the light. As an important example we discuss SWGs etched into silicon-on-insulator wafers for use in integrated photonic circuits; see Fig. 1a. A silicon slab waveguide can be patterned with SWGs of longitudinal, transverse or two-dimensional

periodicity. For periodic longitudinal gratings with periodicity along the axis of propagation, Bragg resonance arises when the period equals the guided half-wavelength, that is,  $\Lambda_{\text{Bragg}} = \lambda_{\text{guided}}/2 = \lambda/(2n_{\text{eff}})$ , where  $n_{\text{eff}}$  is the waveguide mode effective index. In general, from photonic crystal theory<sup>49</sup> it is known that light propagation through a periodic slab waveguide is governed by the dispersion relation shown in Fig. 1b (left). In the diagram, three regimes can be identified: the subwavelength, Bragg and radiation regimes. In the Bragg regime (that is, within the photonic bandgap), no propagating optical mode exists, and a guided wave entering a periodic waveguide in this frequency range decays exponentially within the grating owing to optical reflection. In the radiation regime, the structure acts as a diffraction grating, leading to radiation of the optical power from the waveguide into free space above and below, as seen in Fig. 1b (right). As a consequence of Bloch's theorem, for shorter subwavelength periods, the waveguide (which has discrete translational symmetry) can support localized Floquet–Bloch modes that propagate without loss. The Floquet–Bloch mode is characterized by an electric field that can be expressed along the propagation direction as a plane wave modulated by a periodic amplitude function of the same periodicity as the waveguide. When the grating periodicity is considerably below the wavelength, photonic crystal effects are relatively unimportant. Consistent with effective-medium theory, the structured slab core acts as a homogeneous medium<sup>27</sup>, which is well approximated as a uniaxial crystal<sup>27</sup> with refractive index tensor elements  $n_{xx} = n_{yy} = n_{\parallel}$  and  $n_{zz} = n_{\perp}$  under the coordinate system defined in Fig. 1a. According to equation (1), by adjusting the filling factor,  $a/\Lambda$ , of the grating,  $n_{\parallel}$  and  $n_{\perp}$  can be tuned between the refractive indices of the constituent core (Si) and cladding (SiO<sub>2</sub>) materials, thereby enabling engineering of the metamaterial refractive index locally on the chip. This is further illustrated in Fig. 1b (left), where the red line shows the dispersion relation of a homogeneous slab waveguide with a core refractive index that results from blending the refractive indices of the constituent materials of the SWG slab waveguide. In the long-wavelength limit (small wavenumber  $k$ ), the SWG waveguide is optically equivalent to a homogeneous waveguide with an effective core index determined by the filling factor, whereas considerably deviating behaviour is observed for shorter wavelengths approaching the Bragg resonance. Lossless mode propagation is observed not only in the deep-subwavelength regime, but also throughout a transition region of the dispersion diagram towards the photonic bandgap. This is of practical importance because the feature sizes required for an SWG structure in the transition region make it much more amenable to existing fabrication techniques than a deep-subwavelength structure. The ability to control the dispersion and anisotropy of SWG waveguides in the transition region provides a powerful design tool to engineer the wavevectors of the propagating modes (see Box 1). Gratings in the transition region are also used to manipulate free-space beams<sup>50</sup>.

It is important to keep in mind that in  $k$  space the transition region of the dispersion diagram is adjacent to the Bragg reflection and radiation regimes, and even small deviations from periodicity that introduce additional spatial frequencies into the subwavelength structure can lead to optical transmission losses by reflection and radiation. Such non-periodicities are introduced through unavoidable fabrication imperfections or by necessity when creating waveguide transitions. For example, great care must be taken in the design of SWG waveguide tapers and transitions to photonic wire waveguides to avoid additional losses that can be incurred by perturbing the periodicity. We expect that limiting radiation losses will become an important practical consideration for photonic components based on transformation optics or inverse design techniques<sup>33,51,52</sup>, which generally employ non-periodic subwavelength structures.

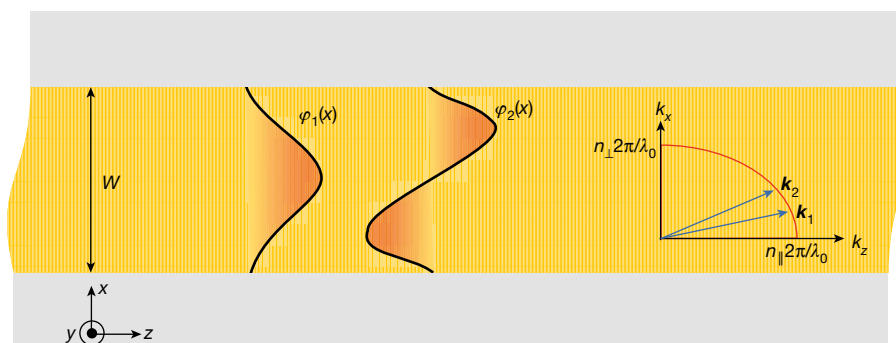
We have described how macroscopic optical material properties, such as birefringence and variable local refractive index profiles, can be artificially generated and engineered by constructing a metamaterial from non-resonant dielectric constituents. In a similar way, creating a metamaterial composed of optically resonant building blocks makes it possible to synthesize artificial bulk materials or surfaces with

## BOX 1

## Waveguiding in an anisotropic material

We consider a multimode waveguide of width  $W$ , made of a uniaxial crystal with refractive indices  $n_{xx}=n_{\parallel}$  and  $n_{zz}=n_{\perp}$  (see figure). The guided modes,  $\varphi_m$ , propagate along the  $z$  direction and are polarized in the  $x$  direction. For the purpose of illustration, we assume strong guiding, so that the optical modes are confined in the waveguide core with a sinusoidal profile,  $\varphi_m(x) \approx \sin(k_{x,m}x)$ , where the lateral wavenumber is given approximately by  $k_{x,m} \approx m\pi/W$  for the  $m$ th guided mode (in the figure,  $m \in \{1, 2\}$ ). The longitudinal component,  $k_{z,m}$ , of the wavevector yields the mode effective index  $n_{\text{eff},m} = k_{z,m}/(2\pi/\lambda)$ , which governs phase matching and beating of the waveguide modes and is thus instrumental in the design of integrated devices. From the elliptical dispersion relation of the crystal,  $(k_{z,m}/n_{\parallel})^2 + (k_{x,m}/n_{\perp})^2 = (2\pi/\lambda)^2$ , and under the paraxial approximation  $k_x \ll 2\pi/\lambda$ , the mode effective indices are found to be  $n_{\text{eff},m} \approx n_{\parallel} - m^2 \lambda^2 n_{\perp}^2 / (8W^2 n_{\parallel}^2)$ . The filling factor and the period of the grating provide control over  $n_{\parallel}$  and  $n_{\perp}$  (see ‘Principles of SWGs’) and, consequently, over the effective index and dispersion of the mode.

In devices based on the multimode interference (Talbot self-imaging) effect, the imaging distance is governed by the beat length,  $L_{\pi}$ , of the two lowest-order modes, that is,  $L_{\pi} = 2\pi/(k_{z,1} - k_{z,2}) \approx 4W^2 n_{\parallel}^2 / (3\lambda n_{\parallel})$ . By engineering the SWG waveguide, the imaging distance can become wavelength-independent, enabling broadband operation<sup>37</sup>.



interesting and often exotic optical properties. Negative-index materials consisting of arrays of split-ring resonators may be the most prominent example<sup>6</sup>. Although homogenization theories are not strictly applicable to common resonant metamaterial structures owing to the length scales involved, a numerical field-averaging study has shown that an effective-medium picture often provides a useful approximation<sup>53</sup>. We have encountered a similar situation in practical non-resonant metamaterials: because of fabrication constraints, the metamaterial does not operate in the deep-subwavelength regime, where effective-medium theory is strictly valid, but in the transition region. Unlike the non-resonant subwavelength waveguides used in integrated optics, resonant metamaterials have mostly been implemented in a planar-optics geometry, with light incident on a metasurface from free space. For example, plasmonic nanoantenna arrays on dielectric substrates allow precise control of optical beams<sup>54</sup>. Because metallic materials generally cause appreciable optical losses, alternative lower-loss materials are being explored<sup>55</sup>. There is also surging interest in all-dielectric resonant metasurfaces using Mie resonators as building blocks to achieve effects such as wavefront shaping, optical Huygens surfaces and magnetic mirrors<sup>14,17,18</sup>. A more detailed discussion of the underlying physical principles of the various resonant metamaterials can be found in a recent review article<sup>22</sup>. An interesting new concept is the use of these resonant metasurfaces on top of planar waveguides to achieve on-chip optical functions such as mode conversion, polarization rotation and asymmetric transmission<sup>56</sup>, thus opening up the prospect of exploiting the properties of resonant metamaterials in integrated optics.

### SWG waveguides and applications

SWG waveguides exploit the ever-improving resolution afforded by complementary metal–oxide–semiconductor (CMOS) lithography techniques, which allow structures with feature sizes below 100 nm to be routinely fabricated in silicon, to locally engineer the material refractive index<sup>24,28</sup>. The straightforward integration of SWG waveguides with planar silicon-strip waveguides, as illustrated in Fig. 2, has enabled a broad range of integrated optical devices with outstanding performance and growing market relevance. A key factor for the

success of SWG structures is their ease of fabrication alongside standard silicon components, typically using lithography with a single full-etch step. The structural period required for subwavelength operation is  $\Lambda < \Lambda_{\text{Bragg}} \approx 300$  nm at telecommunication wavelengths ( $\lambda \approx 1.55 \mu\text{m}$ ). This is well within the range of both electron-beam lithography and wafer-scale deep-ultraviolet lithography, albeit with some limitations in the available filling factors, to comply with the minimum feature sizes of about 50 nm and 100 nm, respectively. For wider (multimode) waveguides with several hundreds of periods, the main fabrication challenge in the short term arises from disorder in the placement of the silicon segments, which changes the translational symmetry of the structure abruptly and must be well below 5 nm to avoid transmission losses<sup>57</sup>. The constraints of minimum feature size and disorder gradually relax for longer wavelengths, making SWG structures particularly promising for the mid-infrared<sup>44,58,59</sup>.

SWG structures open up unique possibilities of advancing the integration of complex functionalities in silicon chips. A crucial first step in this integration is efficient coupling to optical fibres that link the on-chip device to the exterior system, providing, for instance, medium- and long-haul transmission of information in data- and telecommunication networks. Although the strong light confinement of conventional silicon photonic waveguides allows the realization of compact, tightly integrated photonic circuits, it also hampers direct butt-coupling to optical fibres owing to the large mismatch in mode size, by a factor of roughly 600 for a standard SMF-28 optical fibre. By contrast, mode size can be increased in an SWG waveguide, where light is delocalized from the silicon core as the overall refractive index is reduced (see Fig. 2). Thus, by gradually reducing the filling factor and the width of the SWG waveguide as it approaches the chip edge, the mode size and effective index can be matched to the fibre mode. This yields virtually polarization-independent coupling, which is more difficult to achieve with conventional ‘inverse tapers’<sup>60</sup>. The efficiency exceeds 90% over a bandwidth of more than 100 nm at telecommunication wavelengths for a high-numerical-aperture fibre<sup>36</sup>.

For coupling to standard fibres, the silicon substrate must be partially removed to avoid leakage of the expanded mode field into the

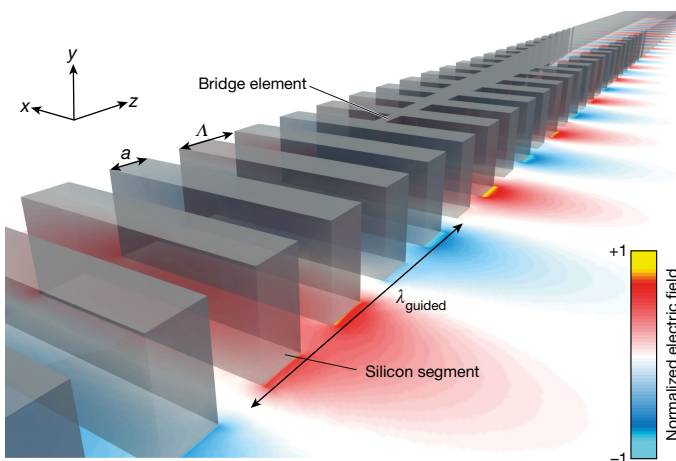


**Fig. 2 | Light propagation in a silicon waveguide with an SWG core.**

In an SWG waveguide the silicon segments (translucent grey blocks) are spaced with a period,  $\Delta$ , smaller than the half-wavelength of the guided light wave,  $\lambda_{\text{guided}}/2$ , so that no diffraction effects arise. Instead, the segmented structure behaves like an anisotropic homogeneous waveguide that blends the refractive indices of the constituent materials, resulting in a reduced mode effective index and an expanded mode size compared to a silicon-strip waveguide. Gradually adding 'bridge' elements in the gaps between the silicon segments provides a nearly lossless transition to the homogeneous silicon waveguide. The colour map shows the normalized electric field of the fundamental horizontally polarized mode.

substrate<sup>61</sup>, as demonstrated by IBM researchers<sup>43</sup>. Such SWG fibre-to-chip couplers can pave the way to efficient, low-cost packaging of silicon photonic chips<sup>62</sup>. An attractive alternative to butt-coupling is offered by surface grating couplers, which operate by diffracting light from the waveguides towards an optical fibre and can thus be placed anywhere on the chip surface. Fully etched grating couplers, apodized with transversal SWGs, have demonstrated peak coupling efficiencies well above 80%<sup>40</sup>, which is considered the threshold for many commercial applications. Without using SWG structures, comparable efficiencies are only achieved with more complex dual-etch-step fabrication processes<sup>63</sup>. Such processes can also be used in combination with sub-wavelength structures to create perfectly vertical grating couplers<sup>64</sup> that allow straightforward packaging. Judicious design of the subwavelength structure can even yield polarization-insensitive couplers, illustrated in Fig. 3a, with the additional ability to focus the light in the chip plane<sup>65</sup>. In these grating couplers, the direction of the free-space-diffracted beam is controlled by manipulating its phase profile by introducing local phase changes at the subwavelength scale, as in a metasurface. Therefore, this type of structure can be regarded as a waveguide grating hybridized with an optical metasurface.

A considerable practical constraint of grating couplers is their limited spectral bandwidth of approximately 35 nm (measured at 1 dB, that is, 80% of maximum efficiency) near a wavelength of 1.55  $\mu\text{m}$ , because the momentum-matching requirement in the grating equation imposes a variation of the diffraction angle with wavelength. This variation is proportional to the grating refractive index. By using SWG structures to decrease the index, a 1-dB bandwidth of 90 nm has been demonstrated, albeit at the expense of coupling efficiency<sup>66</sup>. Thus, achieving simultaneous broadband and high-efficiency operation is a challenge. Prism-assisted SWG couplers could potentially provide such a solution<sup>38</sup>. SWG structures have also been used for coupling light into suspended germanium waveguides at mid-infrared wavelengths<sup>44</sup>, but still with comparatively low efficiencies (around 10%).

Once light is coupled into a nanophotonic waveguide, backscatter arising from the strong interaction of the mode field with the rough sidewalls<sup>67</sup> can pose a major challenge for reflection-sensitive applications, such as on-chip light sources. The delocalization of the mode in an SWG waveguide can be exploited to diminish this interaction and

reduce backscatter by two orders of magnitude<sup>68</sup>, which may alleviate the need for complex on-chip isolators. Likewise, this reduced interaction with the silicon waveguide core reduces the effective nonlinear coefficient in an SWG waveguide by more than a factor of ten compared to a conventional silicon waveguide, thereby suppressing nonlinear impairments and permitting high-speed data transmission<sup>69</sup>. The same principle enables on-chip time delays of the order of tens of picoseconds by using SWG waveguides of identical length but different group indices, synthesized by changes in the duty cycle<sup>41</sup>. It has also been shown that the dispersion profile of such waveguides, with a silicon nitride cladding, can be tailored to obtain both large normal and low anomalous dispersion, which is promising for optical signal processing applications<sup>70</sup>. Furthermore, the periodic nature of the optical field in SWG waveguides (see Fig. 2) creates equally periodic optical forces that can trap nanoparticles both at the sides of the silicon segments and in the gaps between them<sup>71</sup>. The working distance for particle trapping is enhanced by the delocalized mode field in SWG waveguides compared to conventional waveguides.

Although SWG structures in the waveguide core produce mode delocalization, the anisotropy of a judiciously designed SWG cladding can effectively enhance modal confinement. Indeed, when a waveguide core made of an isotropic material is embedded in an anisotropic cladding, total internal reflection requires only that the refractive index of the core material be larger than that of the cladding in the direction perpendicular to the propagation. Counter-intuitively, a large refractive index of the cladding in the direction parallel to the propagation will then increase the decay rate of the evanescent field<sup>72</sup>. Such an anisotropic cladding was implemented by subwavelength patterning (parallel to the direction of propagation) of the waveguide material around the silicon core to demonstrate reduced crosstalk between densely packed waveguides<sup>73</sup>. SWG claddings patterned perpendicular to the direction of propagation are advantageously used for waveguides operating in the mid-infrared, where the silicon dioxide layer that optically insulates the waveguide core from the silicon substrate becomes lossy. The gaps in the SWG cladding allow the removal of the lossy oxide layer using hydrofluoric acid, resulting in suspended waveguides that are laterally supported by the SWG segments<sup>59</sup>. Using this approach, silicon waveguides with losses less than 1 dB  $\text{cm}^{-1}$  at  $\lambda = 3.8 \mu\text{m}$  and 3 dB  $\text{cm}^{-1}$  at  $\lambda = 7.7 \mu\text{m}$ , as well as slotted waveguides with losses of 8 dB  $\text{cm}^{-1}$  at  $\lambda = 2.3 \mu\text{m}$ , have been fabricated<sup>58,59,74</sup>.

## On-chip devices and systems

Devices for on-chip beam splitting, polarization management and spectral filtering are essential building blocks for integrated optical systems, and SWG structures are facilitating key advances in all three areas. Directional couplers are widely used to implement integrated beam splitters. However, their operation principle, which is based on the interference of a pair of supermodes in two parallel waveguides, offers a limited operational bandwidth (about 25 nm at telecommunication wavelengths). Superimposing an SWG structure on a conventional directional coupler provides control over the dispersion of these supermodes and enables operation over a bandwidth of around 100 nm<sup>75,76</sup>. Even broader bandwidths, in excess of 500 nm, can be obtained through the Talbot (self-imaging) effect in multimode SWG waveguides (see Fig. 3b), resulting in a threefold enhancement of the bandwidth compared to conventional devices<sup>37</sup>. This is achieved by taking advantage of the SWG anisotropy to attain a wavelength-independent imaging distance, as outlined in Box 1. Extending this device to four inputs and four outputs, while maintaining excess losses and imbalance below 1 dB, would yield a telecommunication quadrature hybrid with a bandwidth of several hundreds of nanometres. When fabricated with wafer-scale lithography, such a device would enable the production of optical coherent receiver systems covering several optical communication bands at once.

By building on the concept of topology optimization<sup>77,78</sup>, extremely compact beam splitters, with a footprint smaller than  $3 \mu\text{m} \times 3 \mu\text{m}$ , can be achieved using intricate subwavelength structures obtained by

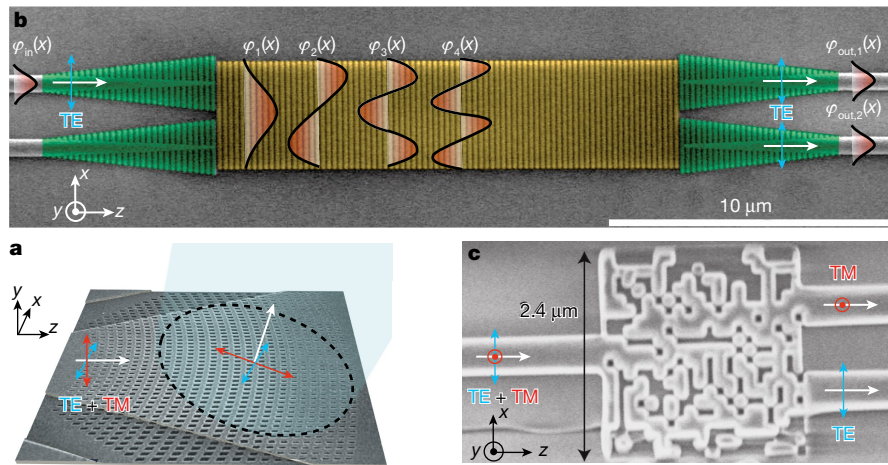


**Fig. 3 | Subwavelength engineered waveguide devices for fibre-to-chip coupling, beam splitting and polarization splitting.** **a**, A focusing, polarization-independent fibre-to-chip grating coupler. Light is coupled from an optical fibre (shown in blue) into the chip ( $x$ - $z$  plane) through a diffraction grating along the  $z$  direction on the chip surface. The grating is curved to provide focusing of the light beam in the chip plane. The SWG (oriented along the  $x$  direction) provides control over the amplitude and phase of the diffracted field, thereby enabling operation at both polarizations, along the  $x$  (transverse electric, TE) and  $y$  (transverse magnetic, TM) directions. Figure adapted from ref. <sup>65</sup>, Optical Society of America. **b**, A broadband on-chip beam splitter based on the multimode interference (Talbot) effect. The input mode,  $\varphi_{in}(x)$ , travels in a silicon-

wire waveguide and is gradually transformed to a wider SWG waveguide mode (green area). At the abrupt transition to the multimode SWG waveguide (yellow area), several higher-order modes are excited and interfere as they propagate, forming images of the expanded input mode. Coupling these images to the output modes ideally yields  $\varphi_{out,1} = \varphi_{in}/\sqrt{2}$  and  $\varphi_{out,2} = i\varphi_{in}/\sqrt{2}$ . By exploiting the anisotropy of the multimode SWG waveguide, the imaging distance can be made almost wavelength-independent, thereby achieving broadband operation (see Box 1). Polarization is transverse electric, that is, in the plane of the chip, along the  $x$  direction. **c**, An ultra-compact polarization beam splitter based on a numerically optimized nanopattern of subwavelength 'pixels' that create a metamaterial. Figure adapted from ref. <sup>52</sup>, Springer Nature Ltd.

numerical minimization techniques, albeit with a more limited bandwidth of about 60 nm<sup>79</sup>. Similar numerical approaches have been used to design ultra-compact devices for on-chip polarization management. One example is a polarization splitter, shown in Fig. 3c, with a footprint of only  $2.4\mu\text{m} \times 2.4\mu\text{m}$  and an extinction ratio of 10 dB over a 30 nm bandwidth<sup>52</sup>. This performance is still limited compared to that of polarization splitters based on bent directional couplers, which offer extinction ratios in excess of 25 dB over a comparable bandwidth but are also about six times longer<sup>80</sup>. Polarization rotation with an extinction ratio of 10 dB, insertion losses of 2 dB and a very competitive 140 nm bandwidth has been recently reported in a 4- $\mu\text{m}$ -long device designed using genetic algorithms<sup>81</sup>. A single device that functions as a polarization splitter with a polarization rotator at one of its outputs has been realized using phase matching between the vertically polarized mode of a silicon wire waveguide and the horizontally polarized mode of an SWG waveguide<sup>82,83</sup>. The device achieves a remarkable tolerance to fabrication deviation of up to  $\pm 40$  nm, whereas many conventional devices tolerate only errors of the order of  $\pm 10$  nm. Thus, compact, practical SWG-based polarization splitters and rotators with extinction ratios above 20 dB and sub-decibel losses with bandwidths over 100 nm seem within reach in the near future<sup>42,84</sup>.

For applications in on-chip spectral filtering, Bragg gratings based on the same principle of successive constructively interfering reflections as their fibre-optic counterparts<sup>85</sup> are commonly used. However, in fully etched nanophotonic waveguides, it is challenging to achieve the low reflection coefficients and long grating lengths required for filtering bandwidths below a few nanometres. This limitation can be overcome by using a waveguide with two corrugations interleaved at the subwavelength scale<sup>86</sup>, which yields a bandwidth of around 1 nm with a resonance depth of 40 dB. Such small bandwidths could previously be achieved in silicon waveguides only in dual-etch-depth designs<sup>87</sup>. Hybrid SWG-Bragg spectral filters with even smaller bandwidths of about 100 pm have recently been proposed<sup>88</sup>. Other structures of interest are contra-directional couplers, which are based on phase-matching modes propagating in two parallel waveguides in different directions via a grating. These couplers offer a wide free spectral range for add-drop wavelength multiplexing but suffer from undesired codirectional

coupling. Using an SWG waveguide in one of the coupler arms promotes contra-directional coupling while producing a strong phase mismatch that efficiently suppresses the codirectional coupling<sup>89</sup>.

System-level integration of SWG structures, while still at an early stage, is already showing outstanding results. Compact Fourier-transform interferometers that synthesize optical path differences using SWG waveguides have been shown to achieve spectral resolution of 50 pm at near-infrared wavelengths<sup>90</sup>. Grating couplers based on two-layer nanostructures and with 92% efficiency have been fabricated using a standard CMOS process<sup>91</sup>, paving the way for system-level integration of electronics and photonic nanostructures<sup>48</sup>.

An outstanding challenge in integrated photonics is achieving dynamic control of the coupling between guided waves and free-space propagating beams. Encouraging results have been reported on waveguide phased arrays<sup>92</sup>, including the first demonstration of coherent solid-state light detection and ranging (LIDAR) using optical phased arrays in a silicon photonics platform<sup>93</sup>. Recent advances in the surging field of optical metasurfaces<sup>16,21,22,54</sup> have also opened prospects for bridging this gap. While the SWG structures that we have discussed typically control the behaviour of light during propagation in the two-dimensional chip plane, the third spatial dimension can be accessed by integrating a metasurface directly on a planar waveguide circuit. This can enable dynamic control of free-space beams emitted off-chip for agile interfacing of integrated optical devices with the external environment. Tuning of the overall metasurface response can be achieved using many different physical mechanisms<sup>22</sup>. Although a planar waveguide circuit with an integrated dynamic metasurface has not yet been demonstrated, several promising candidates have been reported. Independent electrical modulation of both amplitude and phase has been demonstrated, enabling electrical switching of diffracted beams at high frequencies (more than 10 MHz)<sup>94</sup>. In this structure, tunability arises from field-effect modulation of the complex refractive index of the conducting oxide layers incorporated into metasurface antenna elements. Applying an electrical bias between metal and indium tin oxide (ITO) changes the sign of the real part of the dielectric permittivity of ITO. When the relative dielectric permittivity,  $\epsilon_r$ , of ITO is in the epsilon-near-zero region ( $-1 < \epsilon_r < 1$ ), a large

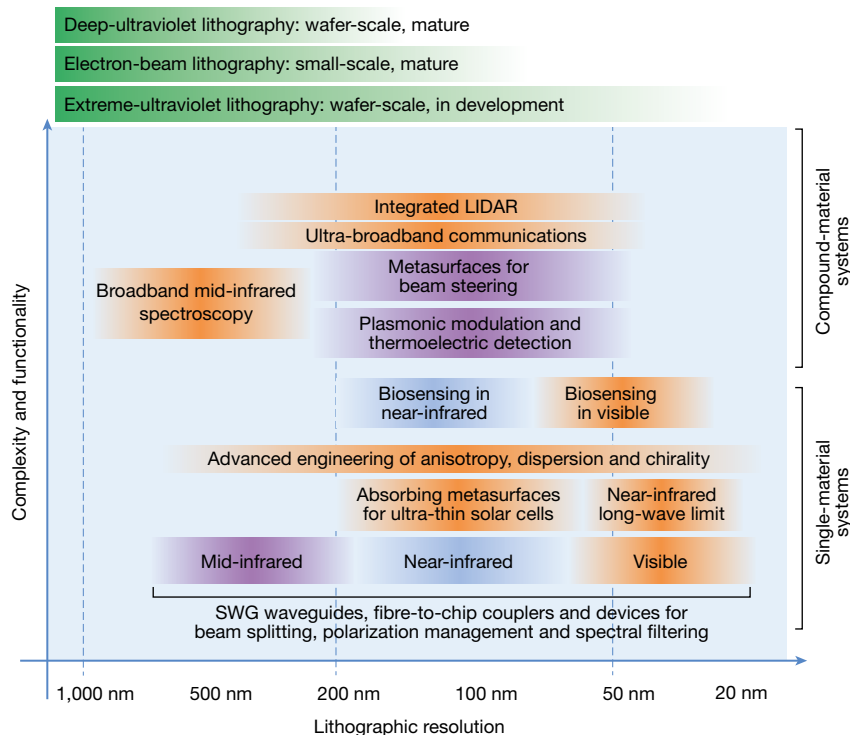


**Fig. 4 | A roadmap for integrated SWG metamaterial devices and systems.** Blue-shaded boxes indicate devices and systems that have already been demonstrated, whereas orange-shaded boxes refer to expected future implementations. Purple boxes show systems for which substantial progress has been made but no waveguide-integrated validation is currently available (beam steering with metasurfaces, plasmonic modulation and thermoelectric detection). In the mid-infrared, some of the functionalities shown (waveguides, fibre-to-chip couplers, beam

splitting) have been implemented, but others have not (polarization management, spectral filtering). The range of feature sizes that can be synthesized with different lithography techniques is indicated by the green bars. We differentiate between systems that can be implemented using a single material (typically silicon) and systems that require additional materials for light generation, detection or active tuning. See ‘Conclusions and outlook’ for a complete description.

electric-field enhancement occurs in the accumulation layer for near-infrared wavelengths, providing an efficient way to electrically modulate the optical phase and amplitude, with high modulation speed and low power consumption. Active metasurfaces have also been explored for electrostatic control of the scattered field phase in the mid-infrared. With active control of phase, one can engineer arbitrary phase fronts in both space and time, enabling dynamically reconfigurable metasurface devices. Electrostatic-phase control in the mid-infrared using graphene- and ITO-integrated resonant structures has demonstrated tunabilities of  $55^\circ$  at  $7.7\ \mu\text{m}$  (graphene)<sup>95</sup> and  $180^\circ$  at  $5.95\ \mu\text{m}$  (ITO)<sup>96</sup>. Recently, a widely tunable phase modulation in excess of  $230^\circ$  was demonstrated using an electrostatically gate-tunable graphene-gold metasurface<sup>97</sup> at  $8.5\ \mu\text{m}$ .

Nanomechanical devices actuated by thermal, electrostatic, magnetic and optical effects can also impact future integrated photonic technologies. Several proof-of-principle demonstrations of nonlinear, switching, electro-optical and magneto-optical functionalities in nanomechanical devices have shown growing potential for practical device integration. This emerging field has recently been reviewed elsewhere<sup>20</sup>.

## Conclusions and outlook

SWG-integrated structures enable the development of a rapidly growing range of high-performance devices at near-infrared telecommunication wavelengths<sup>36,37,40,81,83,86</sup>. The incorporation of these all-dielectric components into more complex, planar waveguide architectures and CMOS processes is expected to continue<sup>68,91,98</sup>, whereas immersion lithography techniques<sup>99</sup> will further facilitate their mass fabrication and commercial exploitation. Some of the SWG structures shown in Fig. 4 have already been successfully brought into the burgeoning field of integrated mid-infrared photonics, including low-loss SWG-engineered waveguides<sup>58</sup> and grating couplers<sup>44</sup>, whereas

others are expected to follow in the near future. In addition, improved lithographic resolution achieved by extreme-ultraviolet techniques<sup>100</sup> will facilitate the use of SWG structures at visible wavelengths and will open up the long-wave limits in the near- and mid-infrared. The flexibility and dispersion-less nature of SWG structures in this regime makes them ideal for the implementation of transformation optics<sup>10</sup>. Furthermore, superior lithographic resolutions would enable the development of SWG-enhanced biosensors in the visible wavelength range, where some of the most sensitive devices reported until now operate<sup>101</sup>. The anisotropic<sup>37,72</sup> and dispersive<sup>70</sup> properties of subwavelength nanostructures, which have barely been explored, offer further research routes in all wavelength ranges. In combination with compound material systems that enable bandgap-free photodecryption<sup>102</sup> and photodetector integration<sup>103</sup>, low-loss SWG waveguides<sup>58</sup> and devices could provide on-chip spectroscopy systems<sup>90</sup> in the mid-infrared fingerprint region, with applications in environmental monitoring and security. Integrated coherent receivers for ultrabroad optical communications are also becoming feasible, with broadband fibre-to-chip couplers already available<sup>36</sup>, and broadband polarization management<sup>81–83</sup> and optical quadrature hybrids<sup>37</sup> within reach. Future on-chip integration of agile metasurfaces reconfigurable at high speeds<sup>94</sup> is envisioned to allow the development of integrated coherent phased arrays at visible and infrared frequencies<sup>93</sup>, enabling functions such as electronic beam steering and focusing, which have previously been available only in microwave RADAR systems.

Received: 18 October 2017; Accepted: 13 June 2018;

Published online 29 August 2018.

1. Rytov, S. M. Electromagnetic properties of a finely stratified medium. *Sov. Phys. JETP* **2**, 466–475 (1956).
2. Mait, J. N. & Prather, D. W. (eds) *Selected Papers on Subwavelength Diffractive Optics* (SPIE Optical Engineering Press, Bellingham, 2001).

3. Lalanne, P., Astilean, S., Chavel, P., Cambriil, E. & Launois, H. Design and fabrication of blazed binary diffractive elements with sampling periods smaller than the structural cutoff. *J. Opt. Soc. Am. A* **16**, 1143–1156 (1999).
4. Bloembergen, N. & Sievers, A. J. Nonlinear optical properties of periodic laminar structures. *Appl. Phys. Lett.* **17**, 483–486 (1970).
5. van der Ziel, J. P. Phase-matched harmonic generation in a laminar structure with wave propagation in the plane of the layers. *Appl. Phys. Lett.* **26**, 60–61 (1975).
6. Smith, D. R., Padilla, W. J., Vier, D. C., Nemat-Nasser, S. C. & Schultz, S. Composite medium with simultaneously negative permeability and permittivity. *Phys. Rev. Lett.* **84**, 4184–4187 (2000).
7. Pendry, J. B. Negative refraction makes a perfect lens. *Phys. Rev. Lett.* **85**, 3966–3969 (2000).
8. Walsler, R. M. Electromagnetic metamaterials. *Proc. SPIE* **4467**, <https://doi.org/10.1117/12.432921> (2001).
9. Shelby, R. A., Smith, D. R. & Schultz, S. Experimental verification of a negative index of refraction. *Science* **292**, 77–79 (2001).
10. Pendry, J. B. Controlling electromagnetic fields. *Science* **312**, 1780–1782 (2006).
11. Fedotov, V. A., Schwanecke, A. S., Zheludev, N. I., Khardikov, V. V. & Prosvirnin, S. L. Asymmetric transmission of light and enantiomerically sensitive plasmon resonance in planar chiral nanostructures. *Nano Lett.* **7**, 1996–1999 (2007).
12. Yen, T. J. et al. Terahertz magnetic response from artificial materials. *Science* **303**, 1494–1496 (2004).
13. Urbas, A. M. et al. Roadmap on optical metamaterials. *J. Opt.* **18**, 093005 (2016).
14. Kuznetsov, A. I., Miroshnichenko, A. E., Brongersma, M. L., Kivshar, Y. S. & Luk'yanchuk, B. Optically resonant dielectric nanostructures. *Science* **354**, aag2472 (2016).
15. Zhu, A. Y., Kuznetsov, A. I., Luk'yanchuk, B., Engheta, N. & Genevet, P. Traditional and emerging materials for optical metasurfaces. *Nanophotonics* **6**, 452–471 (2017).
16. Lalanne, P. & Chavel, P. Metalenses at visible wavelengths: past, present, perspectives. *Laser Photonics Rev.* **11**, 1600295 (2017).
17. Staude, I. & Schilling, J. Metamaterial-inspired silicon nanophotonics. *Nat. Photon.* **11**, 274–284 (2017).
18. Jahani, S. & Jacob, Z. All-dielectric metamaterials. *Nat. Nanotechnol.* **11**, 23–36 (2016).
19. Zheludev, N. I. Obtaining optical properties on demand. *Science* **348**, 973–974 (2015).
20. Zheludev, N. I. & Plum, E. Reconfigurable nanomechanical photonic metamaterials. *Nat. Nanotechnol.* **11**, 16–22 (2016).
21. Genevet, P. & Capasso, F. Holographic optical metasurfaces: a review of current progress. *Rep. Prog. Phys.* **78**, 024401 (2015).
22. Chen, H.-T., Taylor, A. J. & Yu, N. A review of metasurfaces: physics and applications. *Rep. Prog. Phys.* **79**, 076401 (2016).
23. Vivien, L. & Pavesi, L. (eds) *Handbook of Silicon Photonics* (CRC Press, Boca Raton, 2013).
24. Cheben, P., Xu, D.-X., Janz, S. & Densmore, A. Subwavelength waveguide grating for mode conversion and light coupling in integrated optics. *Opt. Express* **14**, 4695–4702 (2006).  
**This paper proposed SWG metamaterial structures for silicon-strip waveguides.**
25. Schmid, J. H. et al. Gradient-index antireflective subwavelength structures for planar waveguide facets. *Opt. Lett.* **32**, 1794–1796 (2007).  
**This study demonstrated SWG structures in a silicon-on-insulator rib waveguide.**
26. Bock, P. J. et al. Subwavelength grating periodic structures in silicon-on-insulator: a new type of microphotonic waveguide. *Opt. Express* **18**, 20251 (2010).
27. Halir, R. et al. Waveguide sub-wavelength structures: a review of principles and applications. *Laser Photonics Rev.* **9**, 25–49 (2015).
28. Cheben, P. et al. Refractive index engineering with subwavelength gratings for efficient microphotonic couplers and planar waveguide multiplexers. *Opt. Lett.* **35**, 2526–2528 (2010).  
**This study demonstrated refractive-index-engineered SWG silicon waveguide devices.**
29. Bock, P. J. et al. Subwavelength grating crossings for silicon wire waveguides. *Opt. Express* **18**, 16146–16155 (2010).
30. Levy, U. et al. Inhomogeneous dielectric metamaterials with space-variant polarizability. *Phys. Rev. Lett.* **98**, 243901 (2007).  
**This paper reported on refractive-index engineering with SWG structures in slab waveguides.**
31. Valentine, J., Li, J., Zentgraf, T., Bartal, G. & Zhang, X. An optical cloak made of dielectrics. *Nat. Mater.* **8**, 568–571 (2009).
32. Hunt, J. et al. Planar, flattened Luneburg lens at infrared wavelengths. *Opt. Express* **20**, 1706 (2012).
33. Gabrielli, L. H. & Lipson, M. Transformation optics on a silicon platform. *J. Opt.* **13**, 024010 (2011).
34. Zentgraf, T., Valentine, J., Tapia, N., Li, J. & Zhang, X. An optical 'Janus' device for integrated photonics. *Adv. Mater.* **22**, 2561–2564 (2010).
35. Glesk, I. et al. All-optical switching using nonlinear subwavelength Mach-Zehnder on silicon. *Opt. Express* **19**, 14031 (2011).
36. Cheben, P. et al. Broadband polarization independent nanophotonic coupler for silicon waveguides with ultra-high efficiency. *Opt. Express* **23**, 22553–22563 (2015).
37. Halir, R. et al. Ultra-broadband nanophotonic beamsplitter using an anisotropic sub-wavelength metamaterial. *Laser Photonics Rev.* **10**, 1039–1046 (2016).  
**This study exploited the anisotropy of SWG structures to achieve broadband operation.**
38. Sánchez-Postigo, A. et al. Broadband fiber-chip zero-order surface grating coupler with 0.4 dB efficiency. *Opt. Lett.* **41**, 3013–3016 (2016).
39. Wangüemert-Pérez, J. G. et al. Evanescent field waveguide sensing with subwavelength grating structures in silicon-on-insulator. *Opt. Lett.* **39**, 4442–4445 (2014).  
**This paper proposed the use of SWG for enhanced waveguide sensing.**
40. Benedikovic, D. et al. Subwavelength index engineered surface grating coupler with sub-decibel efficiency for 220-nm silicon-on-insulator waveguides. *Opt. Express* **23**, 22628–22635 (2015).
41. Wang, J. et al. Subwavelength grating enabled on-chip ultra-compact optical true time delay line. *Sci. Rep.* **6**, 30235 (2016).
42. Xu, Y. & Xiao, J. Ultracompact and high efficient silicon-based polarization splitter-rotator using a partially-etched subwavelength grating coupler. *Sci. Rep.* **6**, 27949 (2016).
43. Barwicz, T. et al. A metamaterial converter centered at 1490nm for interfacing standard fibers to nanophotonic waveguides. In *Proc. Optical Fiber Communication Conference M21.3* (Optical Society of America, 2016).
44. Kang, J. et al. Focusing subwavelength grating coupler for mid-infrared suspended membrane germanium waveguides. *Opt. Lett.* **42**, 2094–2097 (2017).
45. Benedikovic, D. et al. L-shaped fiber-chip grating couplers with high directionality and low reflectivity fabricated with deep-UV lithography. *Opt. Lett.* **42**, 3439–3442 (2017).
46. Flueckiger, J. et al. Sub-wavelength grating for enhanced ring resonator biosensor. *Opt. Express* **24**, 15672–15686 (2016).
47. Yan, H. et al. Unique surface sensing property and enhanced sensitivity in microring resonator biosensors based on subwavelength grating waveguides. *Opt. Express* **24**, 29724–29733 (2016).  
**This work demonstrated enhanced surface sensitivity for SWG waveguides.**
48. Sun, C. et al. Single-chip microprocessor that communicates directly using light. *Nature* **528**, 534–538 (2015).
49. Joannopoulos, J. D., Johnson, S. G., Winn, J. N. & Meade, R. D. *Photonic Crystals: Molding the Flow of Light* 2nd edn (Princeton University Press, Princeton, 2008).
50. Chang-Hasnain, C. & Yang, W. High-contrast gratings for integrated optoelectronics. *Adv. Opt. Photonics* **4**, 379–440 (2012).
51. Piggott, A. Y. et al. Inverse design and demonstration of a compact and broadband on-chip wavelength demultiplexer. *Nat. Photon.* **9**, 374–377 (2015).
52. Shen, B., Wang, P., Polson, R. & Menon, R. An integrated-nanophotonics polarization beamsplitter with  $2.4 \times 2.4 \mu\text{m}^2$  footprint. *Nat. Photon.* **9**, 378–382 (2015).
53. Smith, D. R. & Pendry, J. B. Homogenization of metamaterials by field averaging (invited paper). *J. Opt. Soc. Am. B* **23**, 391 (2006).
54. Kildishev, A. V., Boltasseva, A. & Shalaev, V. M. Planar photonics with metasurfaces. *Science* **339**, 1232009 (2013).
55. Boltasseva, A. & Atwater, H. A. Low-loss plasmonic metamaterials. *Science* **331**, 290–291 (2011).
56. Li, Z. et al. Controlling propagation and coupling of waveguide modes using phase-gradient metasurfaces. *Nat. Nanotechnol.* **12**, 675–683 (2017).
57. Ortega-Moñux, A. et al. Disorder effects in subwavelength grating metamaterial waveguides. *Opt. Express* **25**, 12222–12236 (2017).
58. Penadés, J. S. et al. Suspended silicon waveguides for long-wave infrared wavelengths. *Opt. Lett.* **43**, 795–798 (2018).
59. Penadés, J. S. et al. Suspended silicon mid-infrared waveguide devices with subwavelength grating metamaterial cladding. *Opt. Express* **24**, 22908–22916 (2016).
60. Almeida, V. R., Panepucci, R. R. & Lipson, M. Nanotaper for compact mode conversion. *Opt. Lett.* **28**, 1302 (2003).
61. Sarmiento-Merenguel, J. D. et al. Controlling leakage losses in subwavelength grating silicon metamaterial waveguides. *Opt. Lett.* **41**, 3443–3446 (2016).
62. Barwicz, T. et al. A novel approach to photonic packaging leveraging existing high-throughput microelectronic facilities. *IEEE J. Sel. Top. Quant.* **22**, 455–466 (2016).  
**This study used a metamaterial fibre-chip coupler for IBM's advanced photonic packaging.**
63. Mekis, A. et al. A grating-coupler-enabled CMOS photonics platform. *IEEE J. Sel. Top. Quant.* **17**, 597–608 (2011).
64. Watanabe, T., Ayata, M., Koch, U., Fedoryshyn, Y. & Leuthold, J. Perpendicular grating coupler based on a blazed anti-back-reflection structure. *J. Light Technol.* **35**, 4663–4669 (2017).
65. Cheng, Z. & Tsang, H. K. Experimental demonstration of polarization-insensitive air-cladding grating couplers for silicon-on-insulator waveguides. *Opt. Lett.* **39**, 2206–2209 (2014).
66. Wang, Y. et al. Design of broadband subwavelength grating couplers with low back reflection. *Opt. Lett.* **40**, 4647–4650 (2015).
67. Melati, D., Melloni, A. & Morichetti, F. Real photonic waveguides: guiding light through imperfections. *Adv. Opt. Photonics* **6**, 156 (2014).
68. Peng, B. et al. Metamaterial waveguides with low distributed backscattering in production O-band Si photonics. In *Proc. Optical Fiber Communication Conference Tu3K.3* (Optical Society of America, 2017).  
**This work showed the low-backscatter advantage of SWG waveguides.**

69. Gao, G. et al. Transmission of 2.86 Tb/s data stream in silicon subwavelength grating waveguides. *Opt. Express* **25**, 2918 (2017).
70. Benedikovic, D. et al. Dispersion control of silicon nanophotonic waveguides using sub-wavelength grating metamaterials in near- and mid-IR wavelengths. *Opt. Express* **25**, 19468–19478 (2017).
71. Ma, K., Han, S., Zhang, L., Shi, Y. & Dai, D. Optical forces in silicon subwavelength-grating waveguides. *Opt. Express* **25**, 30876–30884 (2017).
72. Jahani, S. & Jacob, Z. Transparent sub-diffraction optics: nanoscale light confinement without metal. *Optica* **1**, 96–100 (2014).
73. Jahani, S. et al. Controlling evanescent waves on-chip using all-dielectric metamaterials for dense photonic integration. *Nat. Commun.* **9**, 1893 (2018).
74. Zhou, W. et al. Fully suspended slot waveguides for high refractive index sensitivity. *Opt. Lett.* **42**, 1245–1248 (2017).
75. Halir, R., Cheben, P., Xu, D., Schmid, J. H. & Janz, S. Colorless directional coupler with dispersion engineered sub-wavelength structure. *Opt. Express* **20**, 13470–13477 (2012).
76. Wang, Y. et al. Compact broadband directional couplers using subwavelength gratings. *IEEE Photonics J.* **8**, 1–8 (2016).
77. Jensen, J. S. & Sigmund, O. Topology optimization for nano-photonics. *Laser Photonics Rev.* **5**, 308–321 (2011).
78. Frandsen, L. H. et al. Topology optimized mode conversion in a photonic crystal waveguide fabricated in silicon-on-insulator material. *Opt. Express* **22**, 8525 (2014).
79. Lu, L. et al. Inverse-designed single-step-etched colorless 3 dB couplers based on RIE-lag-insensitive PhC-like subwavelength structures. *Opt. Lett.* **41**, 5051–5054 (2016).
80. Wu, H. & Dai, D. High-performance polarizing beam splitters based on cascaded bent directional couplers. *IEEE Photonics Technol. Lett.* **29**, 474–477 (2017).
81. Yu, Z., Cui, H. & Sun, X. Genetic-algorithm-optimized wideband on-chip polarization rotator with an ultrasmall footprint. *Opt. Lett.* **42**, 3093–3096 (2017).
82. Xiong, Y. et al. Polarization splitter and rotator with subwavelength grating for enhanced fabrication tolerance. *Opt. Lett.* **39**, 6931–6934 (2014).
83. He, Y. et al. Silicon polarization splitter and rotator using a subwavelength grating based directional coupler. In *Proc. Optical Fiber Communication Conference Th1G.6* (Optical Society of America, 2017).
84. Xu, L. et al. Polarization beam splitter based on MMI coupler with swg birefringence engineering on soi. *IEEE Photonics Technol. Lett.* **30**, 403–406 (2018).
85. Kashyap, R. *Fiber Bragg Gratings* 2nd edn (Academic Press, Burlington, 2009).
86. Pérez-Galacho, D. et al. Optical pump-rejection filter based on silicon sub-wavelength engineered photonic structures. *Opt. Lett.* **42**, 1468–1471 (2017).
87. Wang, X. et al. Narrow-band waveguide Bragg gratings on SOI wafers with CMOS-compatible fabrication process. *Opt. Express* **20**, 15547 (2012).
88. Čtyroký, J. et al. Design of narrowband Bragg spectral filters in subwavelength grating metamaterial waveguides. *Opt. Express* **26**, 179–194 (2018).
89. Naghdi, B. & Chen, L. R. Silicon photonic contradirectional couplers using subwavelength grating waveguides. *Opt. Express* **24**, 23429–23438 (2016).
90. Podmore, H. et al. Demonstration of a compressive-sensing Fourier-transform on-chip spectrometer. *Opt. Lett.* **42**, 1440–1443 (2017).
91. Notaros, J. et al. Ultra-efficient CMOS fiber-to-chip grating couplers. In *Proc. OFC 2016* 1–3 (IEEE, 2016).
92. Sun, J., Timurdogan, E., Yaacobi, A., Hosseini, E. S. & Watts, M. R. Large-scale nanophotonic phased array. *Nature* **493**, 195–199 (2013).
93. Poulton, C. V. et al. Coherent solid-state LIDAR with silicon photonic optical phased arrays. *Opt. Lett.* **42**, 4091 (2017).
94. Huang, Y. W. et al. Gate-tunable conducting oxide metasurfaces. *Nano Lett.* **16**, 5319–5325 (2016).
- This work demonstrates a gate-tunable metasurface that allows dynamic electrical control of light phase and amplitude, with a modulation frequency greater than 10 MHz.**
95. Dabidian, N. et al. Experimental demonstration of phase modulation and motion sensing using graphene-integrated metasurfaces. *Nano Lett.* **16**, 3607–3615 (2016).
96. Park, J., Kang, J. H., Kim, S. J., Liu, X. & Brongersma, M. L. Dynamic reflection phase and polarization control in metasurfaces. *Nano Lett.* **17**, 407–413 (2017).
97. Sherrott, M. C. et al. Experimental demonstration of >230° phase modulation in gate-tunable graphene-gold reconfigurable mid-infrared metasurfaces. *Nano Lett.* **17**, 3027–3034 (2017).
98. Barwicz, T., Kamlapurkar, S., Martin, Y., Bruce, R. L. & Engelmann, S. A silicon metamaterial chip-to-chip coupler for photonic flip-chip applications. In *Proc. Optical Fiber Communication Conference Th2A.39* (Optical Society of America, 2017).
99. Jeong, S. et al. Low-loss, flat-topped and spectrally uniform silicon-nanowire-based 5th-order CROW fabricated by ArF-immersion lithography process on a 300-mm SOI wafer. *Opt. Express* **21**, 30163–30174 (2013).
100. McGrath, D. ASML claims major EUV milestone. *EETimes* [http://www.eetimes.com/document.asp?doc\\_id=1332012](http://www.eetimes.com/document.asp?doc_id=1332012) (2017).
101. Gavela, A. F., García, D. G., Ramirez, J. C. & Lechuga, L. M. Last advances in silicon-based optical biosensors. *Sensors* **16**, 285 (2016).
102. Mauser, K. W. et al. Resonant thermoelectric nanophotonics. *Nat. Nanotechnol.* **12**, 770–775 (2017).
103. Berini, P. Surface plasmon photodetectors and their applications. *Laser Photonics Rev.* **8**, 197–220 (2014).

**Acknowledgements** We are grateful to S. Janz, D.-X. Xu, A. Ortega-Moñux, Í. Molina-Fernández, J. G. Wangüemert-Pérez, J. Lapointe, J. Čtyroký, C. Alonso-Ramos, D. Benedikovic, G. Mashanovich, A. V. Velasco, W. Ye, M. L. Calvo, L. Vivien, Y. Grinberg, D. Melati and M. Dado for discussions. R.H. acknowledges financial support from Ministerio de Economía y Competitividad, Programa Estatal de Investigación, Desarrollo e Innovación Orientada a los Retos de la Sociedad (cofinanciado FEDER) Proyecto TEC2016-80718-R. H.A.A. acknowledges financial support from the Air Force Office of Scientific Research under grant number FA9550-16-1-0019.

**Author contributions** J.H.S., R.H., P.C. and H.A.A. wrote the manuscript. P.C. and D.R.S. contributed to its preparation.

**Competing interests** The authors declare no competing interests.

#### Additional information

**Reprints and permissions information** is available at <http://www.nature.com/reprints>.

**Correspondence and requests for materials** should be addressed to P.C.

**Publisher's note**: Springer Nature remains neutral with regard to jurisdictional claims in published maps and institutional affiliations.